

Electronically Tunable Transparent Conductive Thin Films for Scalable Integration of 2D Materials with Passive 2D–3D Interfaces

Theresa Grünleitner, Alex Henning,* Michele Bissolo, Armin Kleibert, Carlos A.F. Vaz, Andreas V. Stier, Jonathan J. Finley, and Ian D. Sharp*

A novel transparent conductive support structure for scalable integration of 2D materials is demonstrated, providing an electronically passive 2D–3D interface while also enabling facile interfacial charge transport. This structure, which comprises an evaporated nanocrystalline carbon (nc-C) film beneath nanometer-thin atomic layer deposited AlO_x , is thermally stable and allows direct chemical vapor deposition of 2D materials onto the surface. The combination of spatial uniformity, enhanced charge screening, and low interface defect concentrations yields a tenfold enhancement of MoS_2 photoluminescence intensity compared to flakes on conventional Si/SiO_2 , while also retaining the strong optical contrast for monolayer flakes. Tunneling across the ultrathin AlO_x enables facile interfacial charge injection, which is utilized for high-resolution scanning electron microscopy and photoemission electron microscopy with no detectable charging. Thus, this combination of scalable fabrication and electronic conductivity across a weakly interacting 2D–3D interface opens up new opportunities for device integration and characterization of 2D materials.

interface would enable unprecedented control over (opto)electronic properties of 2D materials and devices. Currently, SiO_2 films on Si serve as the substrates of choice for both chemical vapor deposited and mechanically transferred 2D materials.^[6–9] One major benefit of these Si/SiO_2 substrates is that strong optical contrast between mono- and few-layer 2D materials can be achieved by controlling the thickness of the SiO_2 dielectric film, thereby enabling flakes to be spatially located and the number of layers to be readily determined using nondestructive optical microscopy.^[10–13] While these substrates offer advantages for numerous 2D device applications and enable back-gating of 2D transistors,^[8,14] they also suffer from small gate capacitances defined by the large oxide thickness required to achieve

1. Introduction

2D van der Waals (vdW) materials offer significant promise for application in advanced optoelectronics, quantum technologies, and catalysis.^[1–3] While the extreme sensitivity of 2D materials to the surrounding environment opens unique application prospects,^[4,5] device functionality is limited by the availability of substrates possessing tunable combinations of optical, electronic, and chemical properties. For example, the ability to tailor both dielectric and interfacial transport properties at the 2D–3D

optimal optical contrast. Furthermore, they are poorly suited for realizing electrically driven optical devices and are incompatible with several common characterization techniques, such as X-ray photoelectron spectroscopy (XPS), scanning electron microscopy (SEM), and Kelvin probe force microscopy (KPFM), which rely on fast carrier discharging. These critical gaps can be overcome by the development of a new interface structure that provides optical transparency, tunable gate impedance, and broad compatibility with different substrates and processes, including for direct chemical vapor deposition (CVD) of 2D materials on the surface. Since such support structures must also be chemically inert and ultra-smooth, simultaneously fulfilling all of these requirements represents a significant challenge.

Although transparent conductive films (TCFs), such as indium tin oxide (ITO) and fluorine-doped tin oxide (FTO),^[15] are key components in a broad range of optoelectronic devices,^[15–18] they are susceptible to high temperature instabilities, rendering them unsuitable as substrates for 2D material growth. In addition, TCFs typically have relatively high surface roughnesses (≈ 1 nm),^[16] whereas ultra-smooth surface morphologies and potential landscapes are required for 2D semiconductors to achieve high carrier mobilities, homogeneous carrier densities, and reproducible (opto)electronic characteristics.^[19] To overcome these limitations, graphene-based TCFs were recently investigated for integration into field effect transistors and optical modulators.^[20] Although these systems

T. Grünleitner, A. Henning, M. Bissolo, A. V. Stier, J. J. Finley, I. D. Sharp

Walter Schottky Institute and Physics Department

Technical University of Munich

85748 Garching, Germany

E-mail: alex.henning@wsi.tum.de; sharp@wsi.tum.de

A. Kleibert, C. A.F. Vaz

Swiss Light Source

Paul Scherrer Institute

Villigen PSI CH-5232, Switzerland



The ORCID identification number(s) for the author(s) of this article can be found under <https://doi.org/10.1002/adfm.202111343>.

© 2022 The Authors. Advanced Functional Materials published by Wiley-VCH GmbH. This is an open access article under the terms of the Creative Commons Attribution License, which permits use, distribution and reproduction in any medium, provided the original work is properly cited.

DOI: 10.1002/adfm.202111343

can exploit the high electrical conductivity, mechanical flexibility, and optical transparency of graphene.^[20] single graphene layers have limited sheet carrier concentrations that can be easily screened, limiting their application as gate electrodes. Furthermore, fabrication of large-area graphene-based electronic devices is complex, often requiring transfer processes that can introduce contaminants and structural defects.^[21,22]

Here, we present a novel TCF structure based on conductive and transparent nanocrystalline carbon (nc-C) films that overcome the limitations of existing substrates. Although studied for many decades, nc-C remains largely underexplored as a TCF, including for 2D materials applications. We show that nc-C substrates can be produced on a large scale with tunable sheet carrier concentrations. Using atomic layer deposition (ALD), we conformally coat the nc-C layer with an amorphous aluminum oxide (AlO_x) layer, having a controlled thickness (down to 1 nm and even below^[23,24]). While the conductive ($\rho < 0.01 \Omega \text{ cm}$) and ultrasmooth (rms roughness $\approx 0.2 \text{ nm}$) carbon coating serves as the transparent electrode, the conformal alumina layer acts as a high- k dielectric ($k \approx 7$ ^[25]) spacer with tunable impedance. Of particular relevance to 2D materials, this structure is thermally and chemically stable under typical growth conditions for CVD of transition metal dichalcogenides, with the alumina layer facilitating the nucleation and

growth of single layer MoS_2 flakes. Importantly, when the nc-C/ AlO_x film is deposited on a Si substrate coated with 270 nm SiO_2 , the high optical contrast for discerning single and multi-layer flakes is retained, thereby enabling subsequent analysis and processing. To demonstrate the utility of this structure, we show that 2D flakes can be directly characterized by electron microscopy and spectroscopy techniques, including scanning electron microscopy (SEM), laboratory-based X-ray photoelectron spectroscopy (XPS), and synchrotron-based X-ray photoemission electron microscopy (XPEEM), without charging effects that would otherwise impair such measurements on conventional Si/ SiO_2 supports. This is possible because the AlO_x thickness is within the length scale of tunneling, thereby enabling rapid discharging of the surface layers. Raman spectroscopy shows good crystal quality of MoS_2 and photoluminescence (PL) measurements reveal that the TCF structure yields significantly enhanced MoS_2 PL emission intensity compared to flakes on SiO_2 substrates, which is attributed to a low interfacial defect concentration and effective electronic shielding of charged defects within SiO_2 . Beyond the application of the nc-C/ AlO_x TCF for 2D materials, the presented scheme provides a highly versatile and flexible route to the uniform and scalable deposition of TCFs on other substrates of relevance to thin film optical and electronics applications.

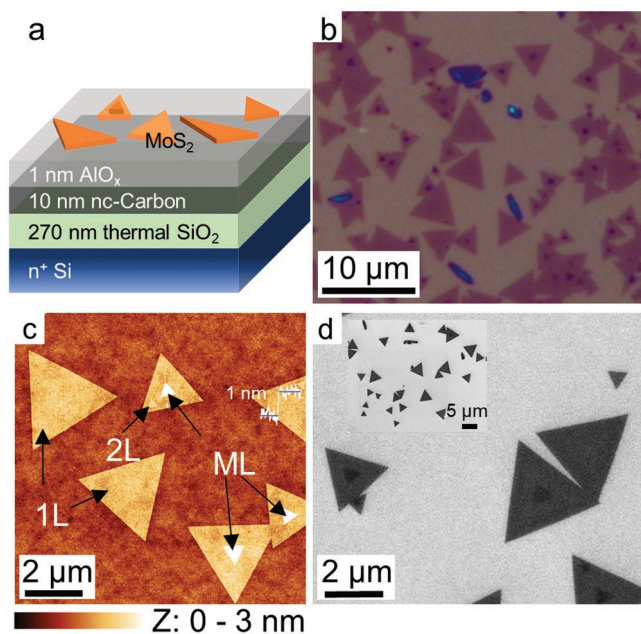


Figure 1. a) MoS_2 (orange) on n^+ Si/thermal SiO_2 substrate coated with a transparent conductive film (TCF) composed of nanocrystalline carbon (nc-C) capped with a 1 nm thin aluminum oxide (AlO_x) layer. The full layer stack is thus given by $\text{Si}/\text{SiO}_2/\text{nc-C}/\text{AlO}_x/\text{MoS}_2$. b) Optical microscopy image of 2D MoS_2 on the structure depicted in (a), demonstrating that high optical contrast of MoS_2 monolayers is retained, despite the presence of the conductive nc-C film. c) AFM image of MoS_2 flakes on the structure, indicating the ultra-smooth and closed nature of the surface following growth of MoS_2 via CVD. The corresponding height profile is shown in white. d) SEM image of MoS_2 on the $\text{Si}/\text{SiO}_2/\text{nc-C}/\text{AlO}_x$ structure, which enables high-resolution imaging without electrical charging effects. The zoomed-out image in the inset further demonstrates the lack of charging-induced artifacts during SEM imaging.

2. Results and Discussion

2.1. Fabrication and Optical Properties of Multi-Layer Structures

Figure 1a illustrates the smooth, conductive, and optically transparent nc-C/ AlO_x structure (hereafter also referred to as the TCF structure), which was deposited onto a Si substrate covered by a 270 nm thick layer of thermal SiO_2 . We note that the Si/ SiO_2 substrate was selected here as a model support that is commonly used to provide excellent optical contrast in 2D materials research, although alternative substrates could also be utilized. The as-deposited structure was probed using atomic force microscopy (AFM) and found to have a low surface roughness ($\approx 0.2 \text{ nm}$).

Following fabrication of the $\text{Si}/\text{SiO}_2/\text{nc-C}/\text{AlO}_x$ structure, MoS_2 was grown on the surface via atmospheric pressure chemical vapor deposition (CVD) at 850°C . Importantly, we found that the complete structure is thermally and chemically stable, withstanding the sulfidizing environment at elevated temperatures during CVD (see below), with the AlO_x layer promoting the nucleation and growth of primarily single layer triangular MoS_2 flakes across its surface, as indicated by the optical micrograph shown in Figure 1b. In addition to confirming the successful growth of MoS_2 , this micrograph highlights that the strong optical contrast between 2D materials and the substrate is retained, despite the presence of the nc-C/ AlO_x TCF structure. Quantification of this contrast $C = \left| \frac{G_{\text{sub}} - G_{\text{MoS}_2}}{G_{\text{sub}}} \right|$,^[26]

where G_{sub} and G_{MoS_2} are the substrate and MoS_2 intensities of the green channel of the RGB mix, respectively, yields values of $C_{\text{TCF}} = 0.28$ for $\text{Si}/\text{SiO}_2/\text{nc-C}/\text{AlO}_x$ (Figure 1b) and $C_{\text{Si/SiO}_2} = 0.26$ for standard Si/SiO_2 substrates (Figure S1, Supporting Information). The retention of strong optical contrast between

the 2D sheets and the underlying substrate is an important feature of the nc-C/ AlO_x TCF that arises from its optical transparency (Figure S2, Supporting Information), which is a consequence of the wide bandgap (>6.5 eV) of the approximately stoichiometric ALD alumina layer (Figures S3 and S4, Supporting Information), as well as the nanocrystalline and ultrathin structure of the carbon film.

Complementary AFM measurements (Figure 1c) confirm the dominant presence of monolayer, crystalline MoS_2 flakes, along with a smaller fraction of bi- and tri-layer regions. Furthermore, AFM reveals that the smooth surface morphology of the underlying TCF structure is preserved after CVD growth, with a roughness of ≈ 0.2 nm (Figure 1c; Figure S5, Supporting Information) that is likely determined by the height variations of the chemomechanically polished Si/SiO_2 substrate (≈ 0.2 nm). We emphasize that a smooth and chemically inert substrate surface is necessary to preserve the intrinsic properties of few- and mono-layer 2D materials because it reduces microscopic strain, while also facilitating the release of strain without distorting the 2D lattice during cooling from the CVD growth temperature.^[27]

For comparison purposes, a 3 nm thin gold coating, deposited by electron-beam evaporation onto a Si/SiO_2 substrate, provides a similar resistivity ($\rho \sim 0.01 \Omega \text{ cm}$) to the nc-C/ AlO_x TCF structure, but has a much higher rms roughness (≈ 1.1 nm) and absorbs light more strongly, thereby reducing the optical contrast of monolayer MoS_2 to 0.17. This comparison highlights the advantages of using nc-C, rather than a metal, as the conductive layer in such a structure.

2.2. Advanced Electron Imaging and Spectroscopy Enabled by Conductive Support

In addition to facilitating CVD growth of MoS_2 , the 1 nm thin AlO_x coating enables charge carriers to tunnel from MoS_2 to the conductive carbon film, as demonstrated by current–voltage measurements with a mercury probe (Figure S6, Supporting

Information). As a consequence, electron microscopy and spectroscopy methods can be readily applied for the characterization of the 2D material. Figure 1d shows a scanning electron microscopy image of individual monolayer MoS_2 flakes on top of the $\text{Si}/\text{SiO}_2/\text{nc-C}/\text{AlO}_x$ structure. No artifacts arising from charging of the 2D material are observed, including at lower magnification (see inset) after initial high-resolution imaging. The resulting SEM images are characterized by sharp features and reveal bilayer nucleation sites within individual monolayer flakes (Figure 1d) that were not always discernable using optical microscopy. In contrast, SEM of MoS_2 on a standard Si/SiO_2 substrate displays significant charging artifacts, which greatly reduce image quality and resolution (Figure S7, Supporting Information).

The utility of the TCF structure for facilitating nanoscale characterization of 2D materials is further highlighted by X-ray photoemission electron microscopy (XPEEM), which is a versatile spectro-microscopic method for nanoscale composition and chemical analysis of surfaces, but requires efficient discharging of the studied material. The $\text{Si}/\text{SiO}_2/\text{nc-C}/\text{AlO}_x$ substrate presented here fulfils this requirement and enables high resolution XPEEM analysis of the local chemical composition of CVD-grown MoS_2 flakes, as shown in Figure 2a,b, in which each pixel represents the integrated area of a single $\text{Mo } 3d_{5/2}$ (Figure 2a) or $\text{Al } 2p$ (Figure 2b) core level spectrum after background subtraction. The large elemental contrast and sharp edges between the MoS_2 triangles (green) and substrate (dark blue) in Figure 2a confirm the lack of electrostatic charging during XPEEM of MoS_2 grown on TCF-coated Si/SiO_2 . The $\text{Al } 2p$ elemental contrast map (Figure 2b) demonstrates the spatial homogeneity of the AlO_x coating of the substrate (green).

The chemical state and purity of CVD MoS_2 on the TCF is further shown by a typical $\text{Mo } 3d$ and $\text{S } 2s$ XPS core level spectrum obtained from a single flake (Figure 2c). The spectrum is dominated by the spin-orbit split doublet at 230.5 and 233.7 eV, corresponding to pristine Mo-S bonding within the material, along with the $\text{S } 2s$ signal at 227.8 eV. The weak doublet having

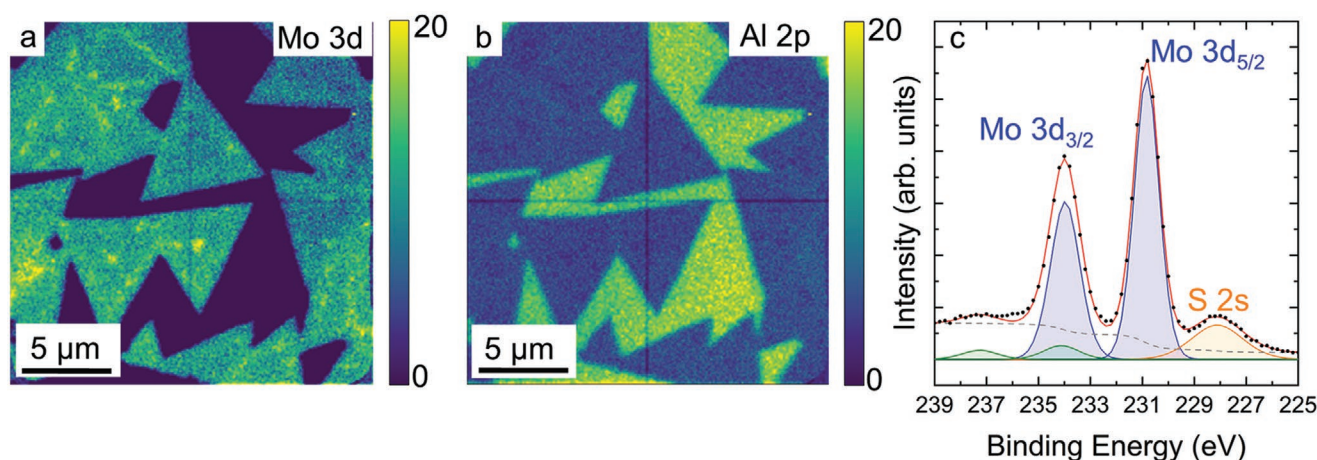


Figure 2. X-ray photoelectron maps of MoS_2 generated by analysis of spatially resolved data from the a) $\text{Mo } 3d$ and b) $\text{Al } 2p$ core level regions. Acquisition of these images with negligible charging was enabled by the $\text{Si}/\text{SiO}_2/\text{nc-C}/\text{AlO}_x$ support, which allows rapid discharging of the surface layers via the conductive nc-C layer. c) A typical $\text{Mo } 3d$ - $\text{S } 2s$ core level spectrum extracted from a sequence of maps acquired with the photon energy ranging from 239 to 225 eV, simultaneously indicating the high chemical quality of the MoS_2 layer grown by CVD and the possibility for high spatial and energy resolution photoemission from supported flakes. Fitted components to the $\text{Mo } 3d$ spectrum are presented in blue (Mo-S), green (Mo-O), and orange (S-Mo), respectively.

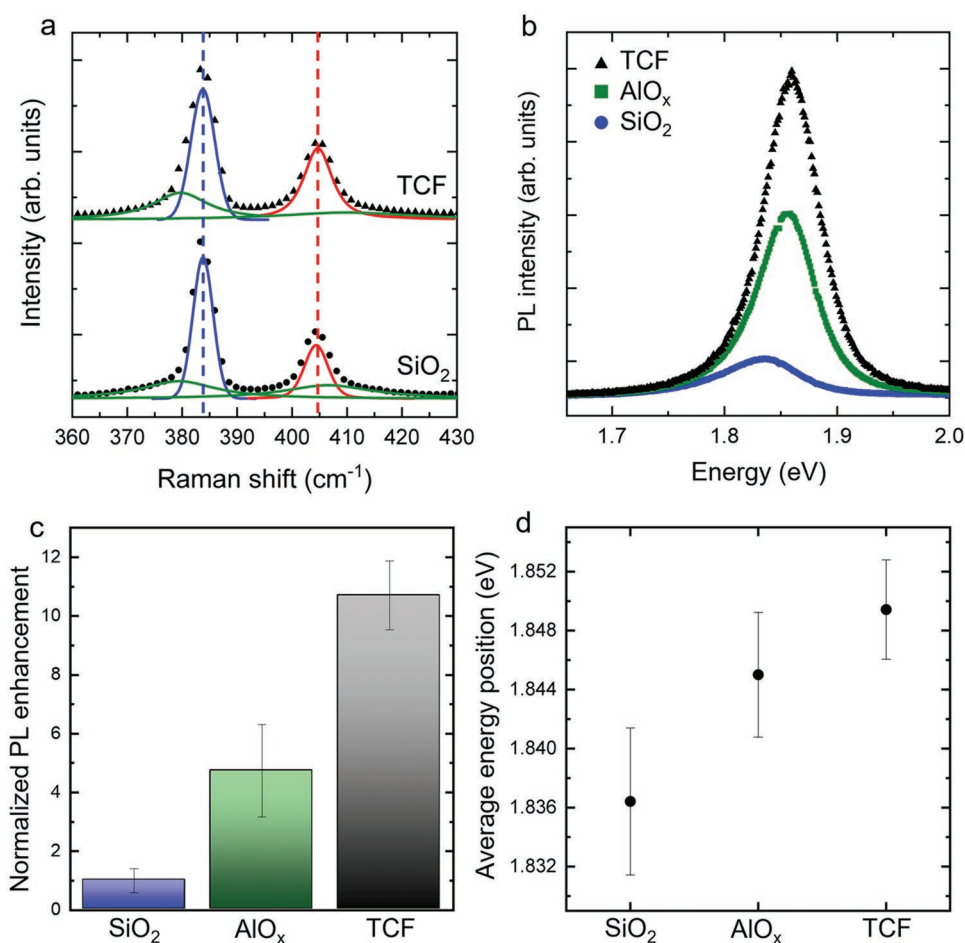


Figure 3. a) Raman spectra of individual MoS₂ flakes on the nc-C/AlO_x TCF structure (triangles) and on SiO₂ (circles). Also included are the fitted E' mode in blue and the A₁' mode in red. The green features are related to disorder-induced Raman modes. The spectra are shifted vertically for better comparison and the vertical lines serve as a guide to the eye. b) Representative PL spectra of individual MoS₂ flakes on the nc-C/AlO_x TCF structure (black triangles), on AlO_x-coated SiO₂ (green squares), and on bare SiO₂ (blue circles) acquired with identical excitation conditions (532 nm, 0.6 mW cm⁻² CW power) at room temperature. Comparison of c) the PL signal intensity and d) peak position from MoS₂ on the different substrates, with error bars indicating the standard deviations from measurements at 15 independent locations on each of the surfaces.

components at 233.8 and 237.0 eV is attributed to Mo-O and has a concentration of <3.5%, which is well below the oxygen concentrations of intentionally doped MoS₂ films reported by Wei et al.^[28] These findings reveal that the 2D MoS₂ is of good quality with minimal oxygen incorporation, doping, or contamination from other chemical species.

2.3. Structural and Optoelectronic Properties of CVD MoS₂ on Conductive Support

To further analyze the structural and optoelectronic quality of the CVD MoS₂ on the TCF, we compare Raman and photoluminescence spectra obtained from individual MoS₂ nanosheets on Si/SiO₂/nc-C/AlO_x substrates to those on standard Si/SiO₂ surfaces. Raman measurements recorded on both substrates (Figure 3a) show that the A₁' and E' Raman modes of the flakes are separated by $\Delta_{\text{TCF}} = 20.94 \pm 0.14 \text{ cm}^{-1}$ ($\Delta_{\text{Si/SiO}_2} = 20.60 \pm 0.10 \text{ cm}^{-1}$), which are characteristic of monolayer MoS₂. The narrow linewidths of the two Raman spectral

features, $\text{FWHM}_{\text{TCF,A}_1'} = 6.16 \pm 0.40 \text{ cm}^{-1}$ and $\text{FWHM}_{\text{TCF,E}'} = 5.13 \pm 0.30 \text{ cm}^{-1}$ ($\text{FWHM}_{\text{Si/SiO}_2,\text{A}_1'} = 5.11 \pm 0.25 \text{ cm}^{-1}$ and $\text{FWHM}_{\text{Si/SiO}_2,\text{E}'} = 4.32 \pm 0.08 \text{ cm}^{-1}$), are fully consistent with previous reports of exfoliated and CVD-grown monolayer MoS₂.^[29,30] These observations reaffirm the high crystal quality of MoS₂ grown on the TCF structure. Since comparison of the peak positions reveals no shift of the Raman modes within the error ($\Delta_{\text{E}'} = 0.03 \text{ cm}^{-1}$, $\Delta_{\text{A}_1'} = 0.31 \text{ cm}^{-1}$) for MoS₂ on the TCF-coated substrate relative to MoS₂ on bare Si/SiO₂, we conclude that an equivalent quality of MoS₂ flakes is achieved on both substrates. Finally, we note that the spectral features at ≈ 380 and 409 cm^{-1} that appear on the left-hand (right-hand) side of the E'(A₁') mode are present in both spectra with similar intensity (Figure 3a). These features are reportedly related to disorder-induced Raman modes at the M point, indicating a similar degree of structural disorder within flakes on both substrates.^[31,32] We note that no spectral signatures characteristic of crystalline Al₂O₃ were detected by Raman spectroscopy, even for 20 nm thick ALD alumina films after annealing at 800 °C.

We continue our analysis of substrate-related optical properties of CVD MoS₂ with PL spectroscopy, which allowed us to probe substrate-induced effects with a higher sensitivity than Raman spectroscopy.^[33] Figure 3b compares PL spectra recorded under comparable excitation conditions from MoS₂ on the TCF and SiO₂ substrates, as well as on AlO_x-coated SiO₂ without the nc-C layer present. The relative intensities, along with their standard deviations from measurements on 15 different spots on each sample, are shown in Figure 3c. Remarkably, the PL intensity for monolayer MoS₂ on the TCF surface increases by more than one order of magnitude compared to the PL intensity of MoS₂ on the regular Si/SiO₂ substrate (Figure 3b,c; Figure S8, Supporting Information). In addition, even in the absence of the nc-C layer, we observed a significant ($\approx 5\times$) increase of the PL intensity on AlO_x. These PL intensity enhancements are accompanied by small blueshifts of the PL maxima from MoS₂ on both the TCF structure (13 meV) and the AlO_x surface (9 meV) compared to the SiO₂ surface (Figure 3d). Since this blueshift is not accompanied by a shift of the Raman A₁' mode position (Figure 3a) or an increase of low energy PL emission due to the negatively charged trion (Figure S8, Supporting Information), we conclude that increased electron doping is unlikely to be the dominant origin of this behavior. Taken together, these data suggest that the PL intensity enhancement for MoS₂ on AlO_x relative to SiO₂ is a consequence of reduced substrate dangling bond defects and covalent interactions.^[34] With the addition of the nc-C layer to form Si/SiO₂/nc-C/AlO_x/MoS₂, we observed an even larger enhancement of the PL intensity, which is consistent with additional screening of charged defect states that are ubiquitous in SiO₂ by the conductive nc-C layer.^[35] These combined effects yield a statistically significant approximately tenfold PL enhancement of MoS₂ on the TCF compared to the reference substrate SiO₂.

2.4. Thermally Induced Transformations of Evaporated Carbon Films

Having demonstrated the applicability of this structure for the growth and characterization of high quality MoS₂, we now turn to the analysis of the basic properties of the nc-C/AlO_x structure, noting that it offers a combination of characteristics that can be broadly useful, potentially reaching beyond 2D material applications. The first fabrication step comprises room temperature deposition of a conformal 10 nm thick amorphous carbon

layer, which is electrically resistive ($\rho > 10 \Omega \text{ cm}$) and smooth (0.17 nm) in its as-deposited state, as summarized in Table 1. As discussed below, the resistivity of this layer is significantly reduced via thermal annealing, including during CVD growth of MoS₂.

Although ALD AlO_x has been previously demonstrated for growth on top of van der Waals materials,^[36,37] this can be challenging since a lack of binding sites could inhibit growth on the evaporated carbon. Thus, we used in situ spectroscopic ellipsometry to track the alumina thickness during ALD on the carbon film with Å-level precision (Figure S9, Supporting Information). The lack of reactive sites on the carbon surface can explain the observed delayed film nucleation (Figure S9, Supporting Information), requiring chemical activation during the first several ALD cycles. However, following this nucleation period, deposition of a nanometer-thin conformal AlO_x coating on the as-deposited amorphous carbon layer was achieved. While charge carriers can directly tunnel through the nanometer-thin AlO_x coating (Figure S6b, Supporting Information), we determined a breakdown electric field of $\approx 5.7 \text{ MV cm}^{-1}$ for a 5.5 nm thick alumina layer (Figure S6c, Supporting Information), which is consistent with literature^[38] and demonstrates the applicability of the nc-C/AlO_x structure for field-effect transistors.

As summarized in Table 1, growth of the ALD layer has a minor impact on the high resistivity of the as-deposited carbon layer. However, we find that annealing at 800 °C in Ar atmosphere transforms the carbon to a smooth nanocrystalline layer with significantly lower resistivity of $1.2 \times 10^{-2} \Omega \text{ cm}$ (Table 1). As shown in Figure S2, Supporting Information, the decreased resistivity is accompanied by a moderate increase of optical absorption, although the material remains optically transparent over a broad spectral range.

To better understand the effect of thermal processing on the structure and resistivity of the carbon film, we performed Raman spectroscopy at different stages in the fabrication of the nc-C/AlO_x TCF. Figure 4 compares the two dominant Raman spectral features of the carbon film, the G peak associated with sp² carbon stretching modes and the D peak associated with a breathing mode of the ring-shaped sp² bonds present in disordered graphite.^[39,40] From analysis of the Raman peak positions and the intensity ratio of the D peak relative to the G peak, I(D)/I(G), one can assess the degree of disorder in the carbon film and estimate the cluster diameter or cluster correlation length, L_a .^[41,42] As illustrated in Figure 4a,b, the peak positions

Table 1. Extracted values from Raman measurements, resistivity, and roughness.

		As-deposited C	C/AlO _x	C/AlO _x Ar annealed	C/AlO _x + CVD MoS ₂
G peak ^{a)}	Peak position [cm ⁻¹]	1545.58	1549.00	1599.31	1600.84
	FWHM [cm ⁻¹]	109.17	96.74	57.12	60.31
D peak ^{a)}	Peak position [cm ⁻¹]	1326.88	1335.27	1358.10	1362.41
	FWHM [cm ⁻¹]	415.32	328.56	297.13	301.80
	I(D)/I(G) ^{a)}	0.41	0.37	1.09	1.08
	Resistivity [$\Omega \text{ cm}$]	1.5×10^6	4.7×10^1	1.2×10^{-2}	
	rms Roughness [nm]	0.17	0.21	0.16	0.16

^{a)}Extracted from Raman measurements.

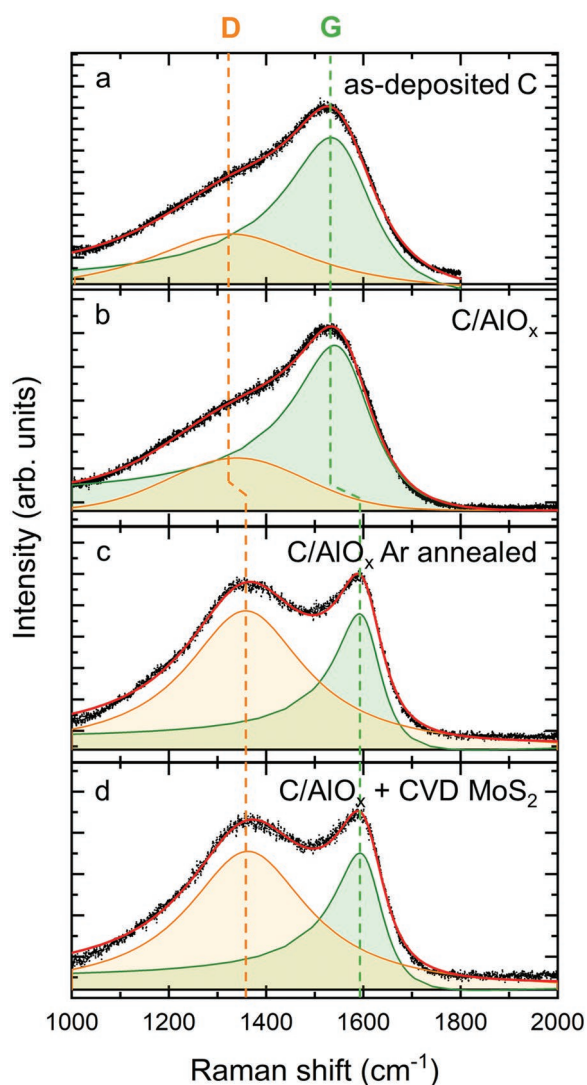


Figure 4. Raman measurements of a) as-deposited C, b) C/AlO_x, c) C/AlO_x annealed in Ar atmosphere, and d) C/AlO_x with CVD-grown MoS₂. The solid red lines represent the cumulated fitted peaks. The G peak is depicted in green, the defect peak D in orange. The vertical dotted lines are a guide to the eye. The TCFs were deposited on Si/SiO₂ substrates.

as well as the intensity ratio, $I(D)/I(G)$, remained nearly constant after AlO_x growth at 200 °C, suggesting that the carbon structure was unaffected by the ALD process. In contrast, after annealing in an Ar atmosphere at 800 °C for 5 min, we observe a strong blueshift of the G peak and an increase of the $I(D)/I(G)$ ratio (Figure 4c and Table 1). Together, these changes indicate formation of graphite nanocrystals via transformation of sp³ bonds to sp² bonds,^[39] as well as clustering of sp² rich regions.^[43] Given prior Raman studies of carbon thin films,^[40] we conclude that the carbon layer is predominantly composed of nanocrystalline graphite (sp² bonds with $L_a \approx 40$ Å) with less than 20% sp³-bonded atoms. This dominant content of graphitic sp² carbon clusters is consistent with the significantly increased conductivities of annealed films^[44,45] (Table 1), as well as the partially reduced optical transparency (Figure S2, Supporting Information). Importantly, performing CVD growth of

MoS₂ yields nearly identical Raman spectra as annealing in Ar (Figure 4d and Table 1), indicating that the conversion of the films to graphitic nc-C occurs similarly under the sulfidizing growth conditions. Advantageous for CVD of 2D materials, no pre-annealing of the substrate was required to achieve the conductive carbon layer during fabrication of the complete Si/SiO₂/nc-C/AlO_x structure.

3. Conclusion

In summary, we have developed a scalable support structure for 2D materials consisting of nanocrystalline carbon coated with an amorphous and conformal ALD-grown AlO_x layer. The structure is smooth, conductive, and optically transparent. The ultrathin conformal AlO_x coating facilitates direct CVD growth of 2D MoS₂ on the surface, while providing an electronically passive 2D–3D interface that also enables facile interfacial charge transport. While the nc-C/AlO_x structure can be applied to various passive or functional substrates, its integration with conventional Si/SiO₂ supports allows the strong optical contrast between single- and multi-layer 2D materials to be retained, while also yielding a strong photoluminescence enhancement. This latter effect is a consequence of low interfacial defect concentrations and screening of charged defect states in the underlying SiO₂ by the conductive nc-C layer. Since ALD allows fabrication of conformal AlO_x high-*k* dielectric spacers of arbitrary thickness down to 1 nm, rapid interfacial charge tunneling across the interface is possible. This feature enables physical, electronic, and chemical characterization using electron imaging and spectroscopy techniques that are otherwise complicated on oxidic supports. As two examples of this, SEM imaging and XPEEM spectromicroscopy are applied to CVD-grown MoS₂ on Si/SiO₂/nc-C/AlO_x supports that simultaneously provide high optical contrast for single layer flakes. In a wider context, the tunability of ALD dielectric coatings provides the opportunity to reliably control interfacial impedance over a wide range while retaining electronically passive and weakly interacting interfaces. Compared to commonly used transparent conductive films and encapsulants, the reported TCF strikes a unique balance of properties, while specifically offering a superior dielectric constant, surface roughness, and ease of fabrication for integration of 2D materials (Table S1, Supporting Information). Furthermore, the deposition process for scalable fabrication of nc-C/AlO_x heterostructures is expected to be broadly compatible with diverse substrates and suitable for applications in numerous optoelectronic applications, extending beyond 2D materials.^[46,47]

4. Experimental Section

Material Deposition: A Quorum Technologies Q150T system featuring pulse evaporation from a carbon rod was used to evaporate a 10 nm thick amorphous carbon (a-C) film on n⁺ Si/SiO₂ substrates. The carbon layer was then coated with AlO_x in a hot-wall plasma-enhanced atomic layer deposition (PE-ALD) reactor (Fiji G2, Veeco CNT) in continuous flow mode at 200 °C. In the first half-cycle, the process was conducted with a base pressure of ≈ 0.09 Torr. Here, ozone was used as the oxidant and trimethylaluminum TMA (electronic grade, 99.999%, STREM

Chemicals) as the precursor for AlO_x and Ar (99.9999%, Linde) as the carrier gas. In the second half-cycle, O_3 was remotely generated using oxygen (99.9999%, Linde) and supplied with 130 ms pulses and peak pressures of ≈ 20 Torr. Each cycle of the TMA/ O_3 process followed the sequence: 80 ms TMA dose, 10 s Ar purge, 130 ms O_3 pulse, 10 s Ar purge. The parameters were implemented so that self-limiting growth occurs, which was controlled by monitoring the film thickness in situ using spectroscopic ellipsometry.

Afterward, single crystalline triangular-shaped MoS_2 was directly grown on top of the $\text{AlO}_x/\text{nc-C}$ thin film. For this process, a home-built chemical vapor deposition (CVD) system was used with a one zone horizontal tube furnace (Nabertherm RS 80/500/11) with a 5 cm inner diameter quartz tube. MoS_2 was grown at ambient pressure (1 atm) with MoO_3 (99.9995%; Alfa Aesar) and S (99.998%; Merck) solid precursors at a target temperature of 850 °C and a flow of 100 sccm of Ar (99.9999%, Linde) as the carrier gas. The TCF on Si/SiO_2 was placed next to the MoO_3 precursor about 17 cm inward from the edge of the furnace. The S precursor was placed upstream of the MoO_3 precursor to obtain a precursor temperature of about 180 °C. The growth time was set to 5 min followed by a natural cool down. For the samples with MoS_2 on the TCF, the annealing of the evaporated carbon happened during the CVD growth process. For all other annealed samples, the same CVD setup and parameters were used without the MoO_3 and S precursors.

In Situ Spectroscopic Ellipsometry: The thickness of the ALD layer was monitored in real-time during the deposition using an in situ spectroscopic ellipsometer (M-2000, J. A. Woollam) and a sampling time of 3 s. The Xenon light source (Hamamatsu, L2174-01) with a spot of $\approx 5 \times 8 \text{ mm}^2$ passed through a fused silica quartz window (Lesker, VPZL-275DU) at an angle of 67°. The data were fit using a general oscillator model.

Atomic Force Microscopy and Scanning Electron Microscopy: AFM images of MoS_2 flakes were acquired using a Bruker Dimension Icon XR (Bruker, USA) AFM in ambient air with platinum silicide (PtSi) probes (Nanosensors). AFM measurements for roughness determination were performed using a Bruker Multimode V microscope (Billerica, MA, USA) in ambient air with NGS30 AFM probes (TipsNano) with a nominal tip radius of 8 nm, typical force constant of 40 N m^{-1} , and resonance frequency of 320 kHz. All images were acquired in tapping mode with a scan rate of 0.5 kHz and 512-point sampling for image sizes of $12 \times 12 \text{ }\mu\text{m}^2$ and $3 \times 3 \text{ }\mu\text{m}^2$. SEM images were collected using a Zeiss NVISION 40 with a secondary electron detector.

Synchrotron X-Ray Photoemission Electron Microscopy: XPS maps were measured at the SIM beamline at the Swiss Light Source (SLS), Paul Scherrer Institut (PSI), by means of X-ray photoemission electron microscopy (XPEEM using a spectroscopic low energy electron microscopy (LEEM) instrument, Elmitec GmbH). During all measurements, a bias of 15 kV was applied between the sample and the objective lens. The spatially resolved X-ray photoelectron spectroscopy images were measured by collecting XPEEM image stacks as a function of photon energy for a fixed value of the energy analyzer (set to 100 eV) to be able to keep the focus settings constant. The kinetic energy of the detected electrons determined the probing depth and was chosen to analyze monolayer MoS_2 . The images were analyzed using a Python script, the Mo 3d core level spectra were extracted from the maps using ImageJ, and the spectra were fitted using CasaXPS. Thereby, the Mo 3d – S 2s core level spectrum (Figure 2c) was calibrated using the adventitious carbon reference peak at 284.8 eV.

Optical Characterization: Raman and PL measurements were performed at room temperature with a 532 nm excitation laser. For all Raman and PL measurements, a home-built Raman setup was used with a Horiba iHR 550 spectrometer (entrance slit 200 μm , 2400 grooves mm^{-1} grating) and liquid nitrogen cooled Horiba Symphony II CCD detector. For the Raman and PL data of MoS_2 , a 100 \times objective lens was used, whereas for the Raman data for the different stages of sample fabrication a 20 \times objective lens was used. All Raman measurements were performed using an excitation power of 5.1 mW, while PL measurements of MoS_2 on Si/SiO_2 and of the TCF were collected at 28 μW . Energy calibration of Raman spectra was carried out using the 520 cm^{-1} Si

Raman line. Raman spectra of MoS_2 were fitted using pseudo-Voigt functions after averaging over three spectra containing an average over 60 sweeps each. The spectra of the nc-C/ AlO_x films were fit using the Breit–Wigner–Fano (BWF) function for all G peaks^[39] and a Lorentzian lineshape for the D peaks. Here, the G peak position was calculated from the fitted peak position, ω_0 , and is smaller than the measured value because ω_0 is due to the undamped mode.^[39]

Electrical Characterization: For the determination of the sheet resistivity, contacts were defined via shadow masks, electrically contacted those with probes mounted on micromanipulators, and measured the voltage drop between the inner contacts while applying a constant current at the outer contacts using a Keithley 2400 source meter unit. For each given resistivity, over four measurements were averaged. A mercury (Hg) droplet (BASI, mercury electrode), operated in a nitrogen atmosphere ($\leq 10 \text{ ppm O}_2$), was used as top electrical contact to characterize out-of-plane charge transport and determine the dielectric breakdown voltage of ALD AlO_x films of the TCFs (Figure S6, Supporting Information). A cross section of the Hg/ $\text{AlO}_x/\text{nc-C}/\text{SiO}_2/\text{Si}$ substrate structure is shown in Figure S6a (Supporting Information).

Supporting Information

Supporting Information is available from the Wiley Online Library or from the author.

Acknowledgements

T.G. and A.H. contributed equally to this work. This work was supported by the DFG through the TUM International Graduate School of Science and Engineering (IGSSE), project FEPChem2D (13.01), and by the Deutsche Forschungsgemeinschaft (DFG, German Research Foundation) under Germany's Excellence Strategy—EXC 2089/1—390776260. A.H. acknowledges funding from the European Union's Horizon 2020 research and innovation programme under the Marie Skłodowska-Curie grant agreement No 841556. The authors acknowledge Prof. Hubert Gasteiger, Simon Qian, and Stefan Oswald from the Chair of Technical Electrochemistry for support with the XPS System. The authors thank J. Primbs for help with the conductivity measurements, M. Zengerle for her help with sample preparation, and S. Wörle for his help with SEM measurements. Part of this work was performed at the Surface/Interface: Microscopy (SIM) beamline of the Swiss Light Source, Paul Scherrer Institut, Villigen, Switzerland.

Open access funding enabled and organized by Projekt DEAL.

Conflict of Interest

The authors declare no conflict of interest.

Data Availability Statement

The data that support the findings of this study are available from the corresponding author upon reasonable request.

Keywords

2D materials, chemical vapor deposition, 2D/3D interfaces, nanocrystalline carbon, transparent conductive films

Received: November 8, 2021

Revised: December 23, 2021

Published online: January 22, 2022

- [1] K. F. Mak, J. Shan, *Nature Photon* **2016**, *10*, 216.
- [2] J. Klein, L. Sigl, S. Gyger, K. Barthelmi, M. Florian, S. Rey, T. Taniguchi, K. Watanabe, F. Jahnke, C. Kastl, V. Zwiller, K. D. Jöns, K. Müller, U. Wurstbauer, J. J. Finley, A. W. Holleitner, *ACS Photonics* **2021**, *8*, 669.
- [3] E. Parzinger, E. Mitterreiter, M. Stelzer, F. Kreupl, J. W. Ager, A. W. Holleitner, U. Wurstbauer, *Appl. Mater. Today* **2017**, *8*, 132.
- [4] M. Florian, M. Hartmann, A. Steinhoff, J. Klein, A. W. Holleitner, J. J. Finley, T. O. Wehling, M. Kaniber, C. Gies, *Nano Lett.* **2018**, *18*, 2725.
- [5] A. V. Stier, N. P. Wilson, G. Clark, X. Xu, S. A. Crooker, *Nano Lett.* **2016**, *16*, 7054.
- [6] P. K. Sahoo, S. Memaran, Y. Xin, L. Balicas, H. R. Gutiérrez, *Nature* **2018**, *553*, 63.
- [7] Y. Huang, Y.-H. Pan, R. Yang, L.-H. Bao, L. Meng, H.-L. Luo, Y.-Q. Cai, G.-D. Liu, W.-J. Zhao, Z. Zhou, L.-M. Wu, Z.-L. Zhu, M. Huang, L.-W. Liu, L. Liu, P. Cheng, K.-H. Wu, S.-B. Tian, C.-Z. Gu, Y.-G. Shi, Y.-F. Guo, Z. G. Cheng, J.-P. Hu, L. Zhao, G.-H. Yang, E. Sutter, P. Sutter, Y.-L. Wang, W. Ji, X.-J. Zhou, H.-J. Gao, *Nat. Commun.* **2020**, *11*, 2453.
- [8] Y. Liu, X. Duan, H.-J. Shin, S. Park, Y. Huang, X. Duan, *Nature* **2021**, *591*, 43.
- [9] S. Shree, I. Paradisanos, X. Marie, C. Robert, B. Urbaszek, *Nat. Rev. Phys.* **2021**, *3*, 39.
- [10] M. M. Benameur, B. Radisavljevic, J. S. Héron, S. Sahoo, H. Berger, A. Kis, *Nanotechnology* **2011**, *22*, 125706.
- [11] P. Blake, E. W. Hill, A. H. Castro Neto, K. S. Novoselov, D. Jiang, R. Yang, T. J. Booth, A. K. Geim, *Appl. Phys. Lett.* **2007**, *91*, 063124.
- [12] X. Dong, A. K. Yetisen, H. Tian, İ. Güler, A. V. Stier, Z. Li, M. H. Köhler, J. Dong, M. Jakobi, J. J. Finley, A. W. Koch, *ACS Photonics* **2020**, *7*, 1216.
- [13] X. Dong, H. Li, Z. Jiang, T. Grünleitner, İ. Güler, J. Dong, K. Wang, M. H. Köhler, M. Jakobi, B. H. Menze, A. K. Yetisen, I. D. Sharp, A. V. Stier, J. J. Finley, A. W. Koch, *ACS Nano* **2021**, *15*, 3139.
- [14] D. Akinwande, C. Huyghebaert, C.-H. Wang, M. I. Serna, S. Goossens, L.-J. Li, H.-S. P. Wong, F. H. L. Koppens, *Nature* **2019**, *573*, 507.
- [15] S. Li, M. Tian, Q. Gao, M. Wang, T. Li, Q. Hu, X. Li, Y. Wu, *Nat. Mater.* **2019**, *18*, 1091.
- [16] Y.-H. Tak, K.-B. Kim, H.-G. Park, K.-H. Lee, J.-R. Lee, *Thin Solid Films* **2002**, *411*, 12.
- [17] A. Way, J. Luke, A. D. Evans, Z. Li, J.-S. Kim, J. R. Durrant, H. K. Hin Lee, W. C. Tsoi, *AIP Adv.* **2019**, *9*, 085220.
- [18] M. Gaillet, L. Yan, E. Teboul, *Thin Solid Films* **2007**, *516*, 170.
- [19] X. Ma, Y. Gong, J. Wu, Y. Li, J. Chen, *Jpn. J. Appl. Phys.* **2019**, *58*, 110905.
- [20] Y. Ma, L. Zhi, *Small Methods* **2019**, *3*, 1800199.
- [21] L. Gao, G.-X. Ni, Y. Liu, B. Liu, A. H. Castro Neto, K. P. Loh, *Nature* **2014**, *505*, 190.
- [22] M. Wang, M. Huang, D. Luo, Y. Li, M. Choe, W. K. Seong, M. Kim, S. Jin, M. Wang, S. Chatterjee, Y. Kwon, Z. Lee, R. S. Ruoff, *Nature* **2021**, *596*, 519.
- [23] L. Wang, J. J. Travis, A. S. Cavanagh, X. Liu, S. P. Koenig, P. Y. Huang, S. M. George, J. S. Bunch, *Nano Lett.* **2012**, *12*, 3706.
- [24] A. Henning, J. D. Bartl, A. Zeidler, S. Qian, O. Bienek, C.-M. Jiang, C. Paulus, B. Rieger, M. Stutzmann, I. D. Sharp, *Adv. Funct. Mater.* **2021**, *31*, 2101441.
- [25] M. D. Groner, J. W. Elam, F. H. Fabreguette, S. M. George, *Thin Solid Films* **2002**, *413*, 186.
- [26] D. Bing, Y. Wang, J. Bai, R. Du, G. Wu, L. Liu, *Opt. Commun.* **2018**, *406*, 128.
- [27] W. H. Chae, J. D. Cain, E. D. Hanson, A. A. Murthy, V. P. Dravid, *Appl. Phys. Lett.* **2017**, *111*, 143106.
- [28] Z. Wei, J. Tang, X. Li, Z. Chi, Y. Wang, Q. Wang, B. Han, N. Li, B. Huang, J. Li, H. Yu, J. Yuan, H. Chen, J. Sun, L. Chen, K. Wu, P. Gao, C. He, W. Yang, D. Shi, R. Yang, G. Zhang, *Small Methods* **2021**, *5*, 2100091.
- [29] Y.-H. Lee, X.-Q. Zhang, W. Zhang, M.-T. Chang, C.-T. Lin, K.-D. Chang, Y.-C. Yu, J. T.-W. Wang, C.-S. Chang, L.-J. Li, T.-W. Lin, *Adv. Mater.* **2012**, *24*, 2320.
- [30] S. Najmaei, Z. Liu, P. M. Ajayan, J. Lou, *Appl. Phys. Lett.* **2012**, *100*, 013106.
- [31] J. Klein, A. Kuc, A. Nölinder, M. Altschneider, J. Wierzbowski, F. Sigger, F. Kreupl, J. J. Finley, U. Wurstbauer, A. W. Holleitner, M. Kaniber, *2D Mater.* **2017**, *5*, 011007.
- [32] S. Mignuzzi, A. J. Pollard, N. Bonini, B. Brennan, I. S. Gilmore, M. A. Pimenta, D. Richards, D. Roy, *Phys. Rev. B* **2015**, *91*, 195411.
- [33] Y. Li, Z. Qi, M. Liu, Y. Wang, X. Cheng, G. Zhang, L. Sheng, *Nanoscale* **2014**, *6*, 15248.
- [34] C. R. Dean, A. F. Young, I. Meric, C. Lee, L. Wang, S. Sorgenfrei, K. Watanabe, T. Taniguchi, P. Kim, K. L. Shepard, J. Hone, *Nat. Nanotech* **2010**, *5*, 722.
- [35] S. Tsoi, P. Dev, A. L. Friedman, R. Stine, J. T. Robinson, T. L. Reinecke, P. E. Sheehan, *ACS Nano* **2014**, *8*, 12410.
- [36] H. Liu, K. Xu, X. Zhang, P. D. Ye, *Appl. Phys. Lett.* **2012**, *100*, 152115.
- [37] N. Li, Z. Wei, J. Zhao, Q. Wang, C. Shen, S. Wang, J. Tang, R. Yang, D. Shi, G. Zhang, *Adv. Mater. Interfaces* **2019**, *6*, 1802055.
- [38] G. Yoo, S. L. Choi, B. Yoo, M. S. Oh, *Phys. Status Solid* **2017**, *214*, 1600619.
- [39] A. C. Ferrari, J. Robertson, *Phys. Rev. B* **2000**, *61*, 14095.
- [40] A. C. Ferrari, J. Robertson, A. C. Ferrari, J. Robertson, *Philos. Trans. R. Soc., A* **2004**, *362*, 2477.
- [41] F. Tuinstra, J. L. Koenig, *J. Chem. Phys.* **1970**, *53*, 1126.
- [42] M. J. Matthews, M. A. Pimenta, G. Dresselhaus, M. S. Dresselhaus, M. Endo, *Phys. Rev. B* **1999**, *59*, R6585.
- [43] S. K. Jerng, D. S. Yu, Y. S. Kim, J. Ryou, S. Hong, C. Kim, S. Yoon, D. K. Efetov, P. Kim, S. H. Chun, *J. Phys. Chem. C* **2011**, *115*, 4491.
- [44] D. Dasgupta, F. Demicheli, A. Tagliaferro, *Philos. Mag. B* **1991**, *63*, 1255.
- [45] A. C. Ferrari, B. Kleinsorge, N. A. Morrison, A. Hart, V. Stolojan, J. Robertson, *J. Appl. Phys.* **1999**, *85*, 7191.
- [46] Y. Zhao, G. Liu, H. Wang, Y. Gao, T. Yao, W. Shi, C. Li, *J. Mater. Chem. A* **2021**, *9*, 11285.
- [47] C. Breazu, M. Socol, N. Preda, O. Rasoga, A. Costas, G. Socol, G. Petre, A. Stanculescu, *Sci. Rep.* **2021**, *11*, 7551.